Coupled spin and valley polarization in monolayer HfN_2 and valley-contrasting physics at the HfN_2-WSe_2 interface

Manish Kumar Mohanta and Abir De Sarkar*
Institute of Nano Science and Technology, Phase 10, Sector 64, Mohali, Punjab-160062, India

(Received 7 June 2020; revised 12 August 2020; accepted 25 August 2020; published 9 September 2020)

Despite extensive studies on coupled spin and valley physics, occurrence of these properties is currently limited to transition-metal dichalcogenides (TMDCs) and graphene. Therefore, exploration of materials beyond TMDCs and graphene is necessary for a further advancement in valleytronics. In this work, the HfN_2 monolayer, a theoretically reported semiconductor having a direct band gap has been investigated in-depth for its applications in valleytronics and spintronics. It exhibits a large valley spin splitting (VSS) ∼314 meV at the conduction band (CB) due to strong spin-orbit coupling (SOC). Such a large VSS at the CB is unique and comparable to that of tungsten-based dichalcogenide monolayers at its valence band (VB). The spin splitting is nearly insensitive to small in-plane strain, whereas the optical transition frequencies between the spin states (ω_{up}, ω_{down}) in the CB and VB is effectively strain tunable. Inspired by the experimentally observed higher exciton lifetime 1.8 ns in $MoSe_2/WSe_2$ type-II van der Waals heterostructure (vdWH) than in the monolayers ∼2.1 (2.5) *ps* in monolayer MoS_2 (WS_2), a type-II (vdWH) prototype has been demonstrated by stacking HfN_2 monolayer over 1H-WSe_2 monolayer for an extended lifetime of valley polarized excitons and large magnitude of spin splitting at both CB and VB. The elastic properties highlight the robustness of HfN_2 monolayer and vdWH, as the bending modulus and critical buckling strain are found to be superior to that in graphene. Further, carrier mobility calculated using the deformation potential theory in HfN_2/WSe_2 is as high as $\mu_h = 16 \times 10^3\,cm^2V^1s^{-1}$. Moreover, this work introduces the HfN_2 monolayer as an exceptionally promising valleytronic material having valley properties complementary to that of Group VI TMDC. This is a report on valley contrasting physics and VSS at the CB, which would strongly motivate experimentalists to synthesize and explore this predicted two-dimensional material.

DOI: 10.1103/PhysRevB.102.125414

I. INTRODUCTION

Two-dimensional (2D) materials have been always at the center stage in research soon after the discovery of graphene in 2004 [1]. A series of 2D materials having a hexagonal honeycomb lattice structure have emerged over time, which show immense potential for their applications in next-generation devices on account of their extraordinary electronic, mechanical, optical, and catalytic properties [2–4]. Among all the exotic properties, the manipulation of intrinsic valley degrees of freedom has been gaining a great deal of popularity in quantum information storage and processing from the perspectives of both fundamental and applied physics [5].

The valley degrees of freedom arise from multiply degenerate energy extrema in the conduction band (CB) or valence band (VB) separated in momentum space. The powerful combination of inversion with time-reversal symmetries ensure Berry curvature and magnetic moments in nonmagnetic centrosymmetric materials, such as graphene, to be zero. Besides, the valleys K and K' can be distinguishable in graphene by breaking the inversion symmetry via stacking of graphene on hexagonal boron nitride [6] or an application of out-of-plane electric field to bilayer graphene [7]. However, the hexagonal nature of two-dimensional (2D) transition metal dichalcogenides (TMDCs) with broken inversion symmetry provides a platform for investigating valley polarization. These materials have two valleys at the K and K' (or -K), which are related to each other by time reversal symmetry [8]. The electrons and holes residing at the K and K' valleys possess opposite spin, orbital magnetic moment, and Berry curvature [9]. The broken inversion symmetry with strong spin-orbit coupling (SOC) introduce valley-contrasting physical properties in TMDC [10]. So far, molybdenum and tungsten based TMDCs have been widely studied for valleytronics as well as spintronics, utilizing their valley and spin degrees of freedom [11–21]. In these systems, the VB undergoes large valley spin splitting which varies from 150 meV in molybdenum-based chalcogenides to 460 meV in tungsten-based chalcogenides [22,23]. With such large valley spin splitting (VSS) in the VB and sizable band gap, the coupled spin and valley physics in 2D TMDCs have been addressed and optically characterized in experiments [24].

To realize a valleytronic device, the balance of charge carriers needs to be broken at K and K' valleys. This can be achieved in numerous ways, as reported theoretically and experimentally [25]. One of the methods is optical excitation by circularly polarized light, which has been extensively used in experiments [13,14,26]. The other approach is to apply a magnetic field to couple to the valley-locked magnetic moments

*abir@inst.ac.in; abirdesarkar@gmail.com

and lift the valley degeneracy via Zeeman splitting which has been experimentally demonstrated in $MoSe_2$ monolayer (0.1–0.3 meV/T) [27–31]. Recent theoretical work demonstrates the role of atomic level doping and magnetic semiconductor substrate in bringing about valley polarization [32–35]. Although significant research progress has been made in 2D TMDC for spintronic and valleytronic applications, other 2D materials having such coupled properties are rarely known or reported.

And to date, all experimentally confirmed 2D valleytronic materials are Group-VI TMDCs where strong SOC leads to large VSS at VB and utilizing spin properties, extensive application in spintronic devices have been experimentally demonstrated. And there are only a few reports on large CB VSS on H-Tl_2O (∼610 meV) by Ma *et al.* [36]. However, Tl_2O is an indirect band gap semiconductor and hence, some intrinsic limitations naturally arise in realizing spin and valley polarization in it. However, in this work, using density functional theory, we have demonstrated the coupled spin and valley polarization in monolayer HfN_2 which is a hexagonal direct band gap semiconductor, where the band energy extrema occur at high symmetry *K* point. The HfN_2 monolayer synergistically combines the desired features of Group IV and VI transition metal dichalcogenide monolayers. In other words, the occurrence of direct band gap at *K* point together with the decoupled band edges [37] provides an important platform for a systematic exploration of spintronic and valleytronic properties in HfN_2 monolayer. It shows strong SOC due to the presence of heavy Hf metal atom. The large valley spin splitting observed at the CB is comparable to that in the 1H-WSe_2 monolayer at its VB. Therefore, the HfN_2 monolayer is expected to serve as the best alternative material to TMDCs in realizing valley and spintronics. Moreover, when HfN_2 monolayer is stacked over 1H-WSe_2 monolayer, valley contrasting physics arises at the interface with a large spin splitting arising at both CB and VB, and an extended lifetime of the valley polarized excitons is expected at type-II van der Waals heterobilayer constituted by these monolayers.

II. COMPUTATIONAL DETAILS

All the electronic properties have been computed using Vienna *Ab* initio Simulation Package (VASP) [38,39]. The projector augmented-wave [40] method has been adopted to describe the ionic potential. The generalized gradient approximation (GGA) [41] in the form of Perdew-Burke-Ernzerhof (PBE) has been used for describing exchange-correlation interaction [41]. The plane wave cut-off energy of 500 eV was used with an energy precision of 10^{-8}eV and a force precision of 2×10^{-2} eV/Å to ensure the convergence in the calculations. A vacuum thickness of 30 Å has been used to avoid the interaction between the periodic images. A Γ-centered *k*-mesh grid of $20 \times 20 \times 1$ has been used for sampling the Brillouin zone. The SOC is included in the band structure calculations to address the relativistic effect, as implemented in VASP. The canonical ensemble-based *ab initio* molecular dynamics (AIMD) simulation is performed at room temperature for 5 ps to confirm the thermal stability of the HfN_2/WSe_2 heterostructure.

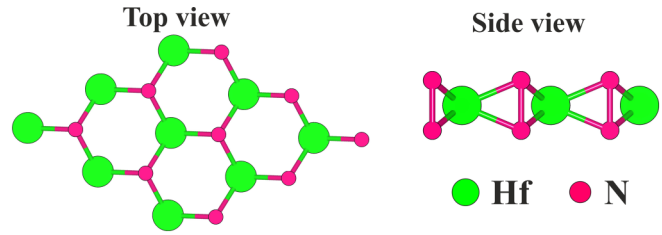

FIG. 1. The top and side view of HfN_2 monolayer

III. RESULTS AND DISCUSSION

The optimized lattice parameters of the theoretically predicted monolayer HfN_2 structure having a hexagonal honeycomb lattice structure have been reported and found to be $a = b = 3.42$ Å. The structure shows $P\bar{6}m2$ symmetry with broken inversion symmetry. The hafnium metal atoms are in trigonal prismatic coordination with six nitrogen atoms, as theoretically predicted by Sun *et al.* [42]. The structure is reported to be stable mechanically and thermodynamically. The top and side views of the structure are presented in Fig. 1.

The electronic band structure calculated using GGA-PBE reveals a direct band gap of 1.44 eV (without SOC) with band edges located at the same high symmetry K point, which is in excellent agreement with the previous report [42]. The spin projected band structure in Fig. 2 clearly shows the valley spin splitting of 314 meV in the CB (Δ_c), whereas the splitting of spin-up and spin-down states near VB (Δ_v) is found to be very small (∼32 meV) upon incorporating the relativistic effect, which is exactly opposite to that of group-VI TMDCs, where large VSS is observed at VB. Such

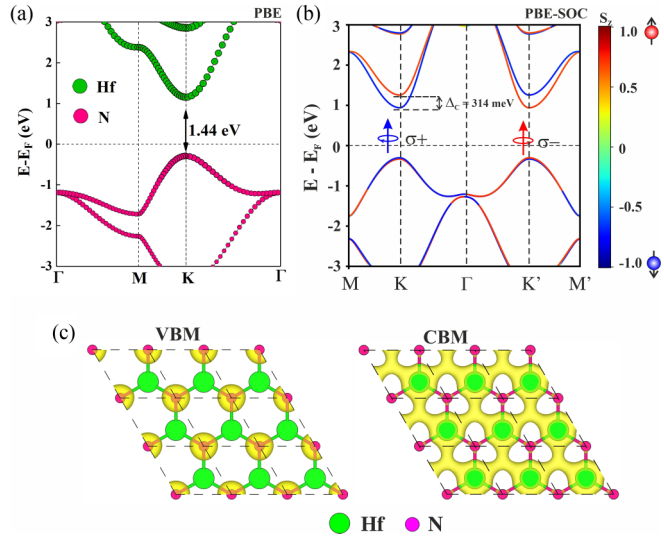

FIG. 2. (a) The calculated atom projected band structure of HfN_2 using GGA-PBE, (b) The spin projected band structure calculated using PBE-SOC and plotted using PYPROCAR [45]. The blue color represents the spin-down state, while red color denotes spin-up state (spin orientation is out-of-plane), (c) band decomposed charge density of VBM and CBM at the *K* point, where the charges are centered around the *N* atom and Hf atom, respectively, with an isosurface value of 0.02 e/Å^3.

VSS in the bands arise due to the composition of bands contributed by heavy (Hf) and light atoms (N) as plotted in the atom-projected band structure and band decomposed charge density, while strong SOC lifts the out-of-plane spin degeneracy of the band edges at K and K' by a significant amount. The VSS in CB observed in HfN_2 ($\Delta_{c(v)} \sim$ 314 (32) meV) is higher than molybdenum based systems and comparable to that of tungsten-based chalcogenides; MoSSe ($\Delta_{c(v)} \sim$ 13.7(170) meV) and WSSe ($\Delta_{c(v)} \sim$ 26.8(449) meV) [43], $MoSe_2$ ($\Delta_v \sim$ 180 meV), WS_2 ($\Delta_v \sim$ 420 meV), and WS_2 ($\Delta_v \sim$ 450 meV) [44]. To gain a deep insight into the physics of spin splitting at the band valleys in HfN_2 monolayer, the orbital contribution has been analyzed. The CB in the vicinity of K, K' is contributed predominantly (88.3%) by Hf (d_{xy}, $d_{x^2-y^2}$), while 11.7% contribution comes from N ($p_{(x,y)}$) orbitals. On the other hand, the VB edge/valleys are consituted mainly (77%) by N ($p_{(x,y)}$) orbitals and partially by Hf (p_z) (23%) orbitals. Hf (d_{xy}, $d_{x^2-y^2}$) orbitals at the CB edge/valleys couple strongly to spin and bring about a large spin splitting at the CB valley in HfN_2 monolayer, which is similar to that of Group VI TMDCs at the VB edge/valleys [23]. Small percentage of Hf ($p_{(z)}$) orbital at the VB edge/valleys is able to interact weakly with spin, resulting in small SOC and spin splitting, which is similar to that of MoS_2 at its CB edge/valleys [23]. The orbital projected band structure of Hf-atom is plotted in Fig. S1 [46] , which clearly shows the orbital composition of band edges. Such large VSS in CB demonstrates its capability for applications in spintronic applications, which is supported by its high charge carrier mobility $\sim 10^3\,\mathrm{cm^2V^{-1}s^{-1}}$ [42].

The $k \cdot p$ Hamiltonian at the band edges in the vicinity of K and K' including spin-orbit coupling is given by [23]

$$H = at(\tau_z k_x \sigma_x + k_y \sigma_y) + \frac{\Delta}{2}\sigma_z - \lambda\tau\frac{\sigma_z - 1}{2}S_z, \qquad (1)$$

where a is the lattice spacing, t is the nearest-neighbor hopping integral, $\tau_z \pm 1$ is the valley index, $\sigma_{x/y/z}$ is the Pauli matrix spanned by the conduction and valence states, S_z is the Pauli matrix for a spin, Δ is the band gap, λ is spin splitting. The Berry curvature in the CB is given by

$$\Omega_c(k) = -\frac{2a^2t^2\Delta}{(4a^2t^2k^2 + \Delta^2)^{\frac{3}{2}}}\tau_z. \qquad (2)$$

The two quantities, Berry curvature ($\Omega_n(k)$) and orbital magnetic moment ($m(k)$) are fundamental quantities in valleytronics [47], where an in-plane electric field is responsible for an anomalous velocity of Bloch electrons perpendicular to the electric field, as given by [8,9]

$$\hbar v_n(k) = \frac{\partial \varepsilon_n(k)}{\partial k} - eE \times \Omega_n(k), \qquad (3)$$

where the second part corresponds to the anomalous velocity proportional to the Berry curvature; $v_a \sim E \times \Omega_n(k)$ [47,48]. The Berry curvature $\Omega_n(k)$ of band n at the **k** point is calculated from the first-principles wave function, using the Kubo formula [49–51] given by

$$\Omega_n(k) = -2\mathrm{Im}\sum_{m\neq n}\frac{\langle\psi_{nk}|\hat{v}_x|\psi_{mk}\rangle\langle\psi_{mk}|\hat{v}_y|\psi_{nk}\rangle}{(E_{nk} - E_{mk})^2}, \qquad (4)$$

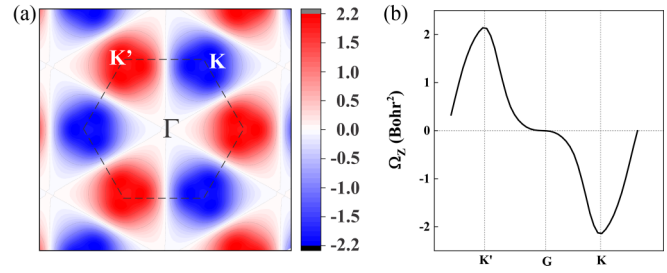

FIG. 3. The Berry curvature (a) as a contour map over the entire 2D Brillouin zone, (b) as a curve along high symmetry points.

where $\hat{v}_{x,y}$ are the velocity operators and the summation are overall the occupied states and plotted along high symmetry K' - Γ - K paths, as shown in Figs. 3(a) and 3(b). As it can be seen in Fig. 3, the nature of the Berry curvature $\Omega(k)$ is completely reversed at the $+K$ and $-K$ (K') valleys due to the time-reversal symmetry $\Omega_n(k) = -\Omega_n(-k)$ [48]. Hence, the Bloch electrons at K and K' will acquire anomalous velocity, and move along opposite directions under the influence of in-plane electric field, which is called the valley Hall effect. Also, the Berry curvature in the VB is equal to that in the CB but with opposite sign $\Omega_{v,k} = -\Omega_{c,k}$. Hence, the optically excited or photogenerated electrons and holes at same K will transport along opposite directions under the application of in-plane electric field. However, the Berry curvature is zero for materials with inversion symmetry. Hence, broken inversion symmetry is necessary for valleytronics.

The contrasting values of $\Omega_n(k)$ and m at the K and K' high symmetry points give rise to selective excitation in the two valleys by photons differing in optical circular helicity. The Berry curvature $\Omega(k)$ and optical circular dichroism $\eta(k)$ are related by

$$\eta(k) = -\frac{\Omega_n(k).\hat{z}}{\mu_B^*(k)}\frac{e}{2\hbar}\Delta(k), \qquad (5)$$

where $\mu_B^* = e\hbar/2m^*$ and $\Delta(k) = (4a^2t^2k^2 + \Delta^2)^{1/2}$ is the direct transition energy, or band gap at k. At the energetic minima at the K and K' points, full selectivity occurs when $\eta(k) = -\tau_z$ [9]. The interband transitions at K valley ($\tau_z = +1$) only couples to right-handed circularly polarized light (RHCP) (σ^+), whereas left-handed circularly polarized light (LHCP) (σ^-) is used to excite the carriers at K' ($\tau_z = -1$), as pictorially shown in Fig. 4(a) [24]. The circularly polarized light cannot only be used to populate the individual valleys but also, the spin-dependent excitation is possible with different optical excitation frequencies. The valleys are separated in momentum space and as a result, the electronic transitions between these discrete valleys of the same energy are energetically forbidden. Hence, the spin valley locking provides a unique opportunity to manipulate different degrees of freedom, which is the basis of next-generation devices, i.e., valleytronics and spintronics for encoding information [9,52]. Equation (5) is valid only for noninteracting interband transitions. For excitons with strong mutual Coulomb interactions, the valley-contrasting optical selection rule is described by nontrivial topological winding number in presence of N-fold rotational symmetry given by $m = w \pm 1 + nN$; where m is

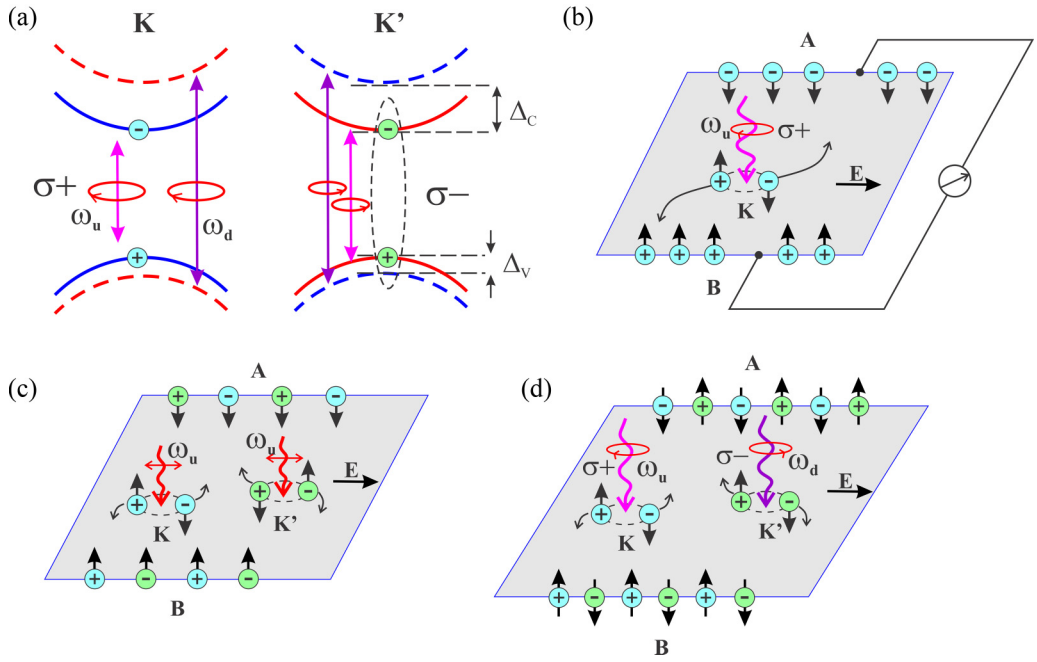

FIG. 4. (a) Spin and valley coupled optical selection rules in HfN_2 The discrete valleys coupled to different circular helicity (σ^+, σ^-) with transition frequencies (ω_u, ω_d), the spin splitting at CB and VB valleys are denoted by $\Delta_{c/v}$, (b) Photoinduced valley Hall effect when circularly polarized light incident on it, where the charge Hall current is spin and valley polarized, (c) Spin and valley Hall effects under linearly polarized optical field with a frequency ω_u, (d) Valley polarization with opposite circular polarization having a frequency ω_u and ω_d.

angular momentum of exciton, w is winding number, and n is the integer [53–55].

The combination of broken inversion symmetry with strong SOC along with the direct band gap having band edges at the high symmetry K point makes HfN_2 monolayer an ideal system to realize valley polarization. Hence, the manipulation of three intrinsic quantum Hall currents; charge, spin, and valley Hall current in monolayer HfN_2 by optical selection rule has been discussed below.

A. Colors and sign convention

"σ^+" represent the RHCP whereas "σ^-" represent LHCP. "+" and "–" in Fig. 4 represent the holes and electrons. "↑ " and "↓ " represents spin-up and spin-down. The cyan color indicates the charge carriers at the K valley whereas the green color represents the same for the K' valley.

B. Spin sign convention

The unoccupied spin-up (-down) state in the VB is referred to as a spin-down (-up) hole [23].

The spin /valley Hall effect has been discussed for HfN_2 monolayer under selective optical field radiation with different polarization and frequency for applications in spintronics and valleytronics.

Referring to Fig. 4(a), under the excitation with RHCP (σ^+) having frequency ω_u ($\sigma^+(\omega_u)$), the spin-down electrons and spin-up holes will be populated in the K valley [23]. And similarly, for $\sigma^+(\omega_d)$ spin-up electrons and spin-down holes will be generated in the same K valley.

When the helicity is reversed to LHCP (σ^-) with frequency ω_u, it will generate spin-up electron and a spin-down hole in the K' valley. And with frequency ω_d, spin-down electron and spin-up holes will be populated in the K' valley. Hence the individual valleys can be populated through the optical selection process.

To populate only the K valley, the sample under study needs to be illuminated with $\sigma^+(\omega_u)$ optical field to generate photoexcited spin-down electrons and spin-up holes. Upon applying an in-plane electric field, they will acquire opposite transverse velocities because of $\Omega_{v,k} = -\Omega_{c,k}$ as stated above and moved to two opposite sides say A and B, as schematically shown in Fig. 4(b). So, the electrons and holes are accumulated at two opposite boundaries of the sample. This will lead to Hall current of valleys, spins, and charges.

The linearly polarized light is the combination of RHCP and LHCP. Hence, it will excite the electrons and holes in both K and K' valleys. Considering linearly polarized light with a frequency ω_u incident on the sample, spin-down electron, and spin-up holes will be generated in the K valley, while spin-up electron and spin-down holes will show up in the K' valley. Considering the carrier dynamics in these discrete valleys, the electrons will move towards side A (say) whereas the holes will move towards B for the K valley excitons and vice-versa for K' valley excitons, as shown pictorially in Fig. 4(c). This will cause the valley Hall effect. Sides A and B corresponding to opposite spins will lead to the spin-Hall effect. But since both electrons and holes are accumulated at both ends of the sample, the charge neutrality will be maintained and hence, the charge Hall current will not be observed. In this case, each boundary will carry a net spin and a valley polarization.

Based on Fig. 4(d), upon irradiating HfN_2 monolayer with optical light with $\sigma^+(\omega_u)$ and $\sigma^-(\omega_d)$, spin-down electrons and spin-up holes will be generated at both K and K' valleys.

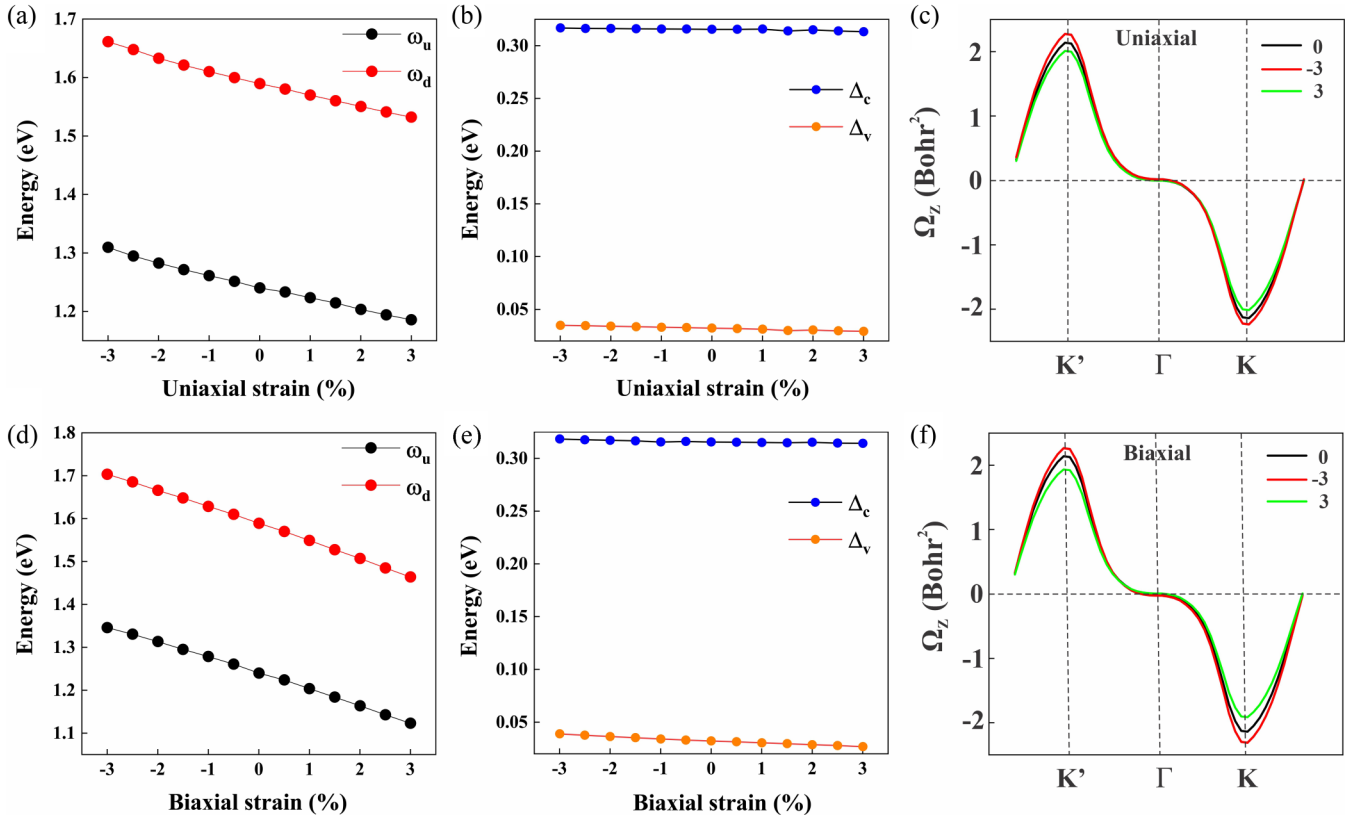

FIG. 5. (a) Strain tunability of optical transition frequency, (b) the variation of spin splitting at CBM and VBM, (c) the evolution of Berry curvature under uniaxial strain, (d)–(f) that for biaxial strain.

The accumulation of photoexcited carriers has been pictorially presented in Fig. 4(d). The spin Hall and charge Hall currents from the electrons will largely cancel out with that of holes in both sides of the Hall bar. However, only valley polarization will be observed in this case. The valley lifetime of an electron can be directly measured with the emission spectra from both the sides after the recombination of the unpolarized electron with spin and valley polarized holes [23].

C. Strain effect on the electronic properties

Strain plays an important role in tuning various electronic, catalytic properties in monolayer TMDs, as evident from many theoretical and experimental studies. For example, theoretical studies predicted the well-known TMDC MoS_2 to transform from direct to indirect band gap at a small 2% uniaxial strain [56]. In this work, both uniaxial and biaxial tensile as well as compressive strain within the range of $\pm 3\%$ has been applied to investigate its effects on the electronic properties. The band structures have been calculated using spin-polarized PBE-SOC and change in various parameters in band structures have been shown in Fig. 5. Under tensile strain, the band gap decreases whereas under compressive strain it increases but remains direct band gap under the specified range of strain.

Figure 5 shows the effect of strain on the optical transition energies (ω_u and ω_d), the spin splitting at CB (Δ_c) and VB (Δ_v), and Berry curvature of the monolayer HfN_2. The optical transition energies (ω_u and ω_d) increase/decrease monotonically with the application of compressive and tensile strain within $+3\%$ to -3%, respectively. The magnitude of spin splitting at the CB is found to be insensitive to the small applied strain, clearly indicating its robustness against mechanical deformation. The spin splitting at VB edge or valleys increases (decreases) under compressive (tensile) strain by a very small magnitude, as shown in Fig. 5. The physical origin of such behavior is attributable to the variation in the degree of contribution by the Hf (p_z) orbital to the VB edge or valleys. As mentioned earlier, this orbital couples weakly to spin, which is responsible for the small spin splitting around the VB edge or valleys. Application of 3% tensile (compressive) strain reduces (increases) the percentage contribution of Hf (p_z) orbital in the VB or valleys by 2% (1.6%), which decreases (increases) the spin-orbit coupling and in turn, the spin splitting at the VB edge by a marginal proportion. The higher (smaller) contribution in % by this orbital accounts for a higher (smaller) SOC and in turn, a larger (smaller) spin splitting. The Chern number C is obtained by integrating the Berry curvature $\Omega(k)$ over the first Brillouin zone [57], $C = \frac{1}{2\pi}\sum_n \int d^2k\ \Omega_n$, has remained zero ($=C_K + C_{K'}$) where K and K' are the two valleys of the honeycomb lattice.

D. Valley contrasting physics in HfN_2/WSe_2 van der Waals heterostructure

Although much effort has been made to explore the materials showing exceptional valley polarization for valleytronics

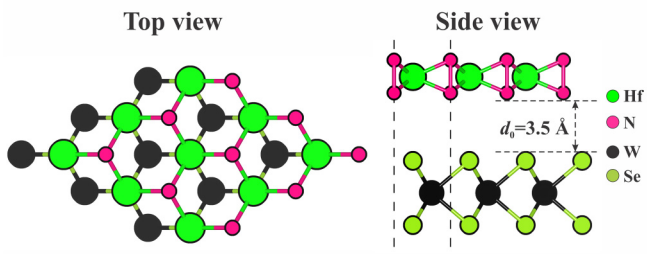

FIG. 6. Top and side view of the optimized geometry of HfN_2/WSe_2 vdWH.

application, the intrinsic limitation of short valley lifetime of excitons in those monolayers ∼2.1 (2.5) *ps* for the MoS_2 (WS_2) monolayer [58,59] hinders realizing their potential valleytronics applications. Recent experiments and theoretical studies on TMDs have shown, the valley lifetime is severely inhibited by the electron-hole exchange interaction [60–62]. However, this issue can be avoided in particular type-II (vdWH) where the CB minimum and VB maximum originate from different layers. Hence the lifetimes of valley excitons get extended as experimentally observed in $WSe_2/MoSe_2$ vdWH (40 ns) [63], 1.8 ns in $MoSe_2/WSe_2$ [64].

In contrast to the above discussion, the 1H-WSe_2 monolayer is chosen as the substrate for the predicted HfN_2 for constructing a van der Waals heterostructure where HfN_2 is stacked over the 1H-WSe_2. The 1H-WSe_2 monolayer is a direct band gap semiconductor having a band gap of 1.53 eV and the band edges are located at high symmetry K point as shown in Fig. S2. In Fig. S2, the valley spin splitting of ∼468/36 meV around VB/CB is observed while the relativistic effects have taken into account. The electronic structure of monolayer WSe_2 with and without SOC has been provided in Fig. S2. Other than WSe_2, experimentally synthesized $MoTe_2$ and a test candidate 1H-WTe_2 has been explored as a suitable substrate for HfN_2 as discussed below.

E. Optimized structure and stability

The optimized interlayer distance between the two layers have obtained from the minima of interlayer distance and binding energy curve [65] as shown in Fig. S3 in the Supplemental Material [46] and found to be 3.5 Å with an interlayer binding energy of $-21.97\,\text{meV/Å}^2$. The top and side view of the optimized geometry is presented in Fig. 6. The thermal stability of the optimized heterostructure has been ascertained by canonical ensemble-based AIMD simulation at room temperature. The snapshot of the final structure with the fluctuation of energy has been plotted in Fig. 7. Moreover, no broken bond has been found in the final structure that confirms experimental feasibility at room temperature. Further, mechanical stability has been confirmed satisfying Born-Huang's stability criteria as discussed in the mechanical properties section below.

F. Electronic properties of the HfN_2/WSe_2 vdWH

The electronic band structure of the optimized geometry calculated using the GGA-PBE functional clearly shows the formation of type-II vdWH with a direct band gap of

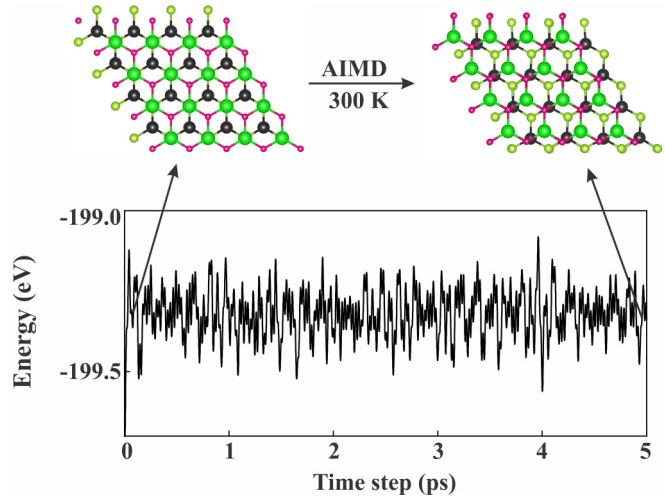

FIG. 7. The snap shot of the final structure along with the energy fluctuation in total energy in molecular dynamics simulation performed at 300 K.

1.36 eV where the CBM and VBM are contributed by HfN_2 and WSe_2 monolayers, respectively, as shown in Fig. 8. Figurre 8(b) clearly shows the Zeeman type spin splitting at K and K' near both the CB and VB edges by including SOC. Although the GGA-PBE exchange-correlation functional underestimates the band gap, it reliably brings out the essential physics and trends. HSE-06 [66] with SOC has been excluded

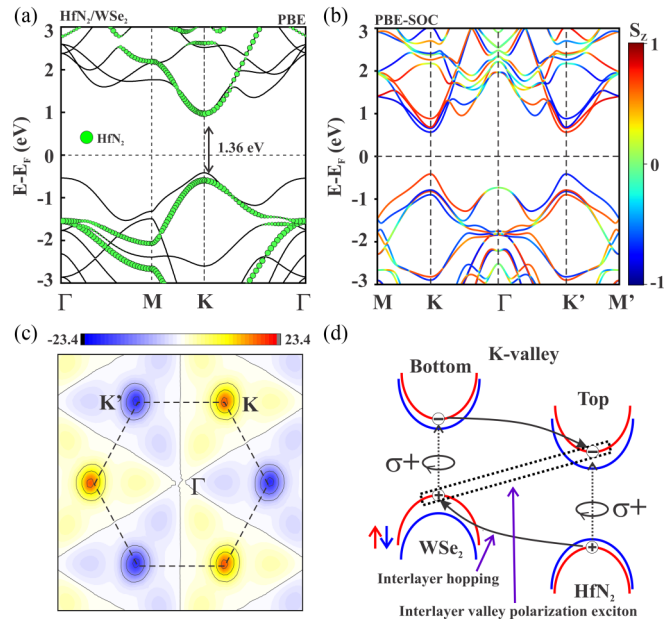

FIG. 8. (a) The electronic band structure of HfN_2/WSe_2 vdWH using GGA-PBE, (b) Spin-resolved band structure projected along the spin orientation S_z incorporating SOC, the red color in the color bar indicates a spin-up state and the blue color indicates a spin-down state, (c) Berry curvature of vdWH associated with VB edge plotted in the k plane, (d) Schematic illustration of the formation of interlayer valley excitons and interlayer hopping within the same spin states and interlayer valley polarization excitons at the K valley of the vdWH. The σ^+ is the right-handed circularly polarized light.

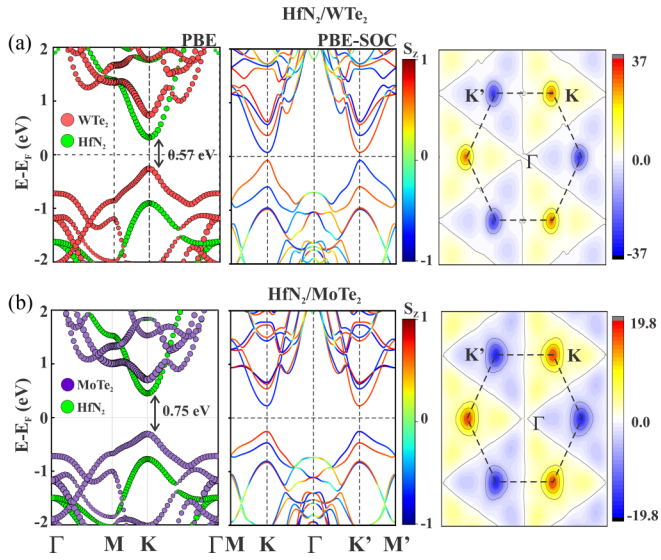

FIG. 9. Electronic band structure using GGA-PBE functional with and without including spin-orbit coupling and Berry curvature associated with VB of (a) HfN_2/WTe_2 and (b) $HfN_2/MoTe_2$ vdWH.

here because of its huge computational cost. The novelty of constructing this vdWH is seen in the band structure plotted in Fig. 8(b), where the nearly equal magnitude of spin splitting at both CB and VB is realized by interfacing these two semiconductors, which would be highly suitable for futuristic applications in valleytronics. The Berry curvature ($\Omega_z(k)$) associated with VB of the vdWH is calculated including SOC and plotted in the k plane as shown in Fig. 8(c). The opposite Berry curvature at K and K' results in both electrons and holes contributing to Hall conductivity or magnetization [67,68]. Apart from the above stacking pattern, two more stacking patterns have been studied, as provided in Fig. S4, where type-II band alignment is noticed; however, a slight variation in band gap is observed across the stacking patterns. The interlayer binding energies are close to each other in all the three stacking orders studied in this work.

G. Principle of action or working mechanism

At the K valley, resonant photoexcitation with right circularly polarized light will selectively excite the electron-hole pair (i.e., exciton) in the WSe_2 monolayer and the ultrafast electron transfer process [69] in type-II vdWH will move electrons to the HfN_2 monolayer, which is known as interlayer hopping within same spin states, thereby leaving the holes behind in the WSe_2 monolayer, as shown in Fig. 8(d) [67]. These valley-polarized excitons can have an extended lifetime due to the suppression of radiative recombination and exchange interaction as the electrons and holes are spatially separated in the two individual monolayers in the van der Waals heterobilayer [61,62,70]. Since the band offsets in the CB edges and the VB edges between the two individual monolayers are very small, external perturbations, such as, strain and electric field, will play a significant role in the alteration of its electronic properties [71].

The choice of a suitable substrate with tunable and desired properties is very important from an experimental point of view. To address the role of substrate, HfN_2 has been supported over 1H-$MoTe_2$ and 1H-WTe_2 monolayers, one at a time, as illustrated below in Fig. 9. 1H-WTe_2 is chosen apart from $MoTe_2$ because of its highest spin splitting ~485 meV among all the TMDCs at the VB edge. As evident from the band structure, HfN_2 forms a type-II band alignment with the above-mentioned TMDCs, while the band gap in the vdWH varies with the substrate. Band offsets between two constitutent monolayers in HfN_2/WSe_2 are very small at both CB and VB edges, whereas appreciable band offset is observed at the other two vdWH, i.e., HfN_2/1H-MTe_2 (M = Mo, W). Moreover, a large VSS is noticed at both CB and VB edges in these two vdWHs.

H. Elastic properties of monolayers and vdWH

The knowledge of elastic properties is essential for practical applications of the material in modern technology. Hence, all the mechanical properties including bending modulus, critical buckling strain, and intrinsic strength have been thoroughly investigated. The elastic constants C_{ij} have been evaluated from the strain-energy curve [72,73] as implemented in the VASPKIT code [74]. It is found to be in excellent agreement with the reported values [42]. The 2D layer modulus, which represents the resistance of a nanosheet to stretching, is given by [75,76]

$$\gamma^{2D} = \tfrac{1}{2}[C_{11} + C_{12}], \tag{6}$$

while Young's modulus (Υ) $= \frac{C_{11}^2 - C_{12}^2}{C_{11}}$, Poisson ratio ($\nu$) $= C_{12}/C_{11}$, and Shear modulus (G) $= C_{66}$. Furthermore, the intrinsic strength (σ_{int}) and bending modulus (D) of a nanosheet can be derived using Refs. [65,76] $\sigma_{\text{int}} \sim \frac{\Upsilon}{9}$, $D = \frac{\Upsilon h^2}{12(1-\nu^2)}$ where h is the thickness of the nanosheet ($h_{\text{HfN2}} = 1.674$ Å, $h_{\text{WSe2}} = 3.36$ Å, $h_{\text{HfN2/WSe2}} = 8.5$ Å). The elastic constants obtained for the monolayers as well as vdWH satisfy Born-Huang stability criteria and other mechanical properties are tabulated in Table I.

Born-Huang stability criteria:

$$C_{11} > |C_{12}|, \quad C_{22} > 0, \quad C_{66} > 0, \quad C_{11}C_{22} - C_{12}^2 > 0.$$

TABLE I. The calculated mechanical stiffness constants C_{ij}, layer modulus (γ^{2D}), Young's modulus (Υ), Poisson's ratio (ν), intrinsic strength (σ_{int}), bending modulus (D) of monolayers, and vdWH

System	C_{11} (N/m)	C_{12} (N/m)	C_{66} (N/m)	γ^{2D} (N/m)	Υ (N/m)	ν	σ_{int} (N/m)	D (eV)
HfN_2	151.54	83.93	33.80	117.73	105.06	0.55	11.67	2.19
WSe_2	145.331	40.051	52.640	92.691	134.29	0.27	14.92	8.5
HfN_2/WSe_2	331.704	129.50	101.102	230.602	281.14	0.39	31.23	124.57

TABLE II. Calculated effective mass (m^*), deformation potential E_i(eV), carrier mobility μ($cm^2V^{-1}s^{-1}$) for electrons and holes along high symmetry directions at 300 K

System	High symmetry Direction	Charge Carrier	$\lvert m^*/m_o\rvert$	$\lvert E_i\rvert$	μ [Lang *et al.* [77]]
HfN_2	K $\rightarrow$ Γ	Electron	0.561	2.9	1179
		Hole	0.876	0.88	5927
	$K \rightarrow M$	Electron	0.589	2.9	1123
		Hole	0.722	0.88	7192
WSe_2	K $\rightarrow$ Γ	Electron	0.382	9.22	239.3
		Hole	0.487	4.27	650.81
	$K \rightarrow M$	Electron	0.416	9.22	219.73
		Hole	0.590	4.27	537.2
HfN_2/WSe_2	K $\rightarrow$ Γ	Electron	0.587	3.16	2020.7
		Hole	0.469	1.34	16153
	$K \rightarrow M$	Electron	0.607	3.16	1954.1
		Hole	0.576	1.34	13152

The critical buckling strain (ϵ_c) of a 2D material can be derived using $\epsilon_c = -\frac{4\pi^2 D}{\Upsilon L_o^2}$, where L is the length of the 2D nanosheet in the unit of Å. For the same length L (in Å), the critical buckling strain for the isolated monolayers and vdWH are found to be $\epsilon_c^{HfN_2} = -\frac{13.17}{L^2}$, $\epsilon_c^{WSe_2} = -\frac{40}{L^2}$, $\epsilon_c^{HfN_2/WSe_2} = -\frac{280.22}{L^2}$.

The bending modulus (2.19 eV) and high buckling strain of monolayer HfN_2 have been calculated and found to be more robust as compared to graphene [76]. Hence, the HfN_2 monolayer will show higher resistance against all kinds of mechanical deformation. The calculated bending modulus of HfN_2/WSe_2 vdWH was found to be ~124 eV compared to that of graphene/MoS_2 (~252 eV) [76] vdWH showing robust mechanical properties.

I. The charge carrier mobility of vdWH

The charge carrier mobility of HfN_2 monolayerhas been calculated to be $\sim 10^3\ cm^2V^{-1}s^{-1}$ in the earlier report [42]. Furthermore, the carrier mobility of the vdWH has been evaluated using the formulation of Lang *et al.* [77,78], which is the improvised version of the one originally proposed by Bardeen and Shockley [79,80] based on deformation potential theory [81–83]:

$$\mu_x = \frac{e\hbar^3\left(\frac{5C_{11}+3C_{22}}{8}\right)}{k_B T (m_x)^{\frac{3}{2}} (m_y)^{\frac{1}{2}} \left(\frac{9E_{1x}^2+7E_{1x}E_{1y}+4E_{1y}^2}{20}\right)}, \tag{7}$$

where $m^*_{x/y}$ are the direction-dependent effective masses, T is set to room temperature (300 K), E_i is the deformation potential calculated from the linear fitting of CBMs and VBMs with respect to the infinitesimal uniaxial lattice dilation, and compression along a particular direction, as shown in the Supplemental Material in Fig. S5 [46]. The elastic constants C_{ij} have been tabulated in Table I. The carrier mobility along with the related parameters of HfN_2/WSe_2 are tabulated in Table II and that for HfN_2/WTe_2 are provided in Fig. S6, Tables S1, and S2.

Such a large carrier mobility $\sim 16 \times 10^3\ cm^2V^{-1}s^{-1}$ along with direct band gap HfN_2/WSe_2 type-II heterostructure is very interesting, not only for valleytronics application but also for nano/optoelectronics and other device-based applications.

IV. CONCLUSION

In summary, valleytronic properties in HfN_2 monolayer have been observed. It combines the best of the properties in Group VI and IV transition metal dichalcogenide (TMDC) monolayers. It is a direct band gap semiconductor, where the CB minimum (CBM) and the VB maximum (VBM) are located at high symmetry K point similar to Group VI TMDC monolayers. While the band edges are decoupled as found in Group IV TMDC monolayers. The strong SOC lifts the out-of-plane spin degeneracy at the band edges where the large valley spin splitting is observed at the CB, in contrast to Group VI TMDC monolayers, where spin splitting occurs at the VB. The large spin splitting near the CB ~315 meV in this hexagonal monolayer with broken inversion symmetry structure is of prime importance in the valley and spin dynamics in nanoscale physics. On the other hand, manipulation of all three intrinsic degrees of freedom (a charge, spin, valley) has been demonstrated via the optical selection rule for next-generation quantum information encoding. The spin splitting is found to be insensitive to a small magnitude of applied strain. However, the optical transition frequencies are effectively tunable via application of strain without affecting the spin splitting. A type-II van der Waals heterostructure (vdWH) prototype has been constructed by interfacing HfN_2 and 1H-WSe_2 monolayers, where large spin splitting at both CB and VB is realized. And the exciton valley lifetime is extendable in this vWH due to spatial separation of electrons and holes in the individual monolayers, which in turn, will enhance the performance of the valleytronic based devices. As a result, unusual valley contrasting physics shows up at this interface. Vertical strain can be utilized in tuning the electronic properties in HfN_2/WSe_2 van der Waals heterobilayer (vdWH). The mechanical properties indicate the structural robustness of the HfN_2 monolayer and the designed vdWH against mechanical deformation. And the high charge carrier mobility $\sim 10^3\ cm^2V^{-1}s^{-1}$ of HfN_2 monolayer and $16 \times 10^3\ cm^2V^{-1}s^{-1}$ for HfN_2/WSe_2 vdWH make them ideal materials for their integration into next-generation valleytronics, spintronics, and nanoelectronics. Hence, once the HfN_2 monolayer is synthesized, its superior properties will push it far ahead of the traditional transition metal dichalcogenide

monolayers in the realm of next-generation quantum electronic devices.

ACKNOWLEDGMENTS

M. K. M. acknowledges the Ph.D. fellowship from Grant No. 09/1129(0007)/2017-EMR-I from the Council of Scientific and Industrial Research (CSIR), India. We acknowledge the financial support provided by the Grant No. SR/NM/NS-1125/2016 from DST (Nanomission) and infrastructural cum fellowship support is given by the Institute of Nano Science and Technology (INST), India. We are grateful to the Centre for Development in Advanced Computing (C-DAC), Pune, India for providing its supercomputing resources on PARAM-YUVA-II and INST for in-house HPC-cluster.

[1] K. S. Novoselov, A. K. Geim, S. V. Morozov, D. Jiang, Y. Zhang, S. V. Dubonos, I. V. Grigorieva, and A. A. Firsov, Science **306**, 666 (2004).
[2] P. Miró, M. Audiffred, and T. Heine, Chem. Soc. Rev. **43**, 6537 (2014).
[3] S. Siahrostami, C. Tsai, M. Karamad, R. Koitz, M. García-Melchor, M. Bajdich, A. Vojvodic, F. Abild-Pedersen, J. K. Nørskov, and F. Studt, Catal. Lett. **146**, 1917 (2016).
[4] D. Akinwande, C. J. Brennan, J. S. Bunch, P. Egberts, J. R. Felts, H. Gao, R. Huang, J.-S. Kim, T. Li, Y. Li, K. M. Liechti, N. Lu, H. S. Park, E. J. Reed, P. Wang, B. I. Yakobson, T. Zhang, Y.-W. Zhang, Y. Zhou, and Y. Zhu, Extreme Mech. Lett. **13**, 42 (2017).
[5] F. Bussolotti, H. Kawai, Z. E. Ooi, V. Chellappan, D. Thian, A. L. C. Pang, and K. E. J. Goh, Nano Futures **2**, 032001 (2018).
[6] R. V. Gorbachev, J. C. W. Song, G. L. Yu, A. V. Kretinin, F. Withers, Y. Cao, A. Mishchenko, I. V. Grigorieva, K. S. Novoselov, L. S. Levitov, and A. K. Geim, Science **346**, 448 (2014).
[7] M. Sui, G. Chen, L. Ma, W.-Y. Shan, D. Tian, K. Watanabe, T. Taniguchi, X. Jin, W. Yao, D. Xiao, and Y. Zhang, Nat. Phys. **11**, 1027 (2015).
[8] D. Xiao, W. Yao, and Q. Niu, Phys. Rev. Lett. **99**, 236809 (2007).
[9] X. Xu, W. Yao, D. Xiao, and T. F. Heinz, Nat. Phys. **10**, 343 (2014).
[10] Y. Ye, J. Xiao, H. Wang, Z. Ye, H. Zhu, M. Zhao, Y. Wang, J. Zhao, X. Yin, and X. Zhang, Nat. Nanotechnol. **11**, 598 (2016).
[11] W. Liu, C. Luo, X. Tang, X. Peng, and J. Zhong, AIP Adv. **9**, 045222 (2019).
[12] S. Wu, J. S. Ross, G.-B. Liu, G. Aivazian, A. Jones, Z. Fei, W. Zhu, D. Xiao, W. Yao, D. Cobden, and X. Xu, Nat. Phys. **9**, 149 (2013).
[13] K. F. Mak, K. He, J. Shan, and T. F. Heinz, Nat. Nanotechnol. **7**, 494 (2012).
[14] H. Zeng, J. Dai, W. Yao, D. Xiao, and X. Cui, Nat. Nanotechnol. **7**, 490 (2012).
[15] B. Zhu, H. Zeng, J. Dai, Z. Gong, and X. Cui, Proc. Natl. Acad. Sci. USA **111**, 11606 (2014).
[16] N. Jena, Dimple, R. Ahammed, A. Rawat, M. K. Mohanta, and A. De Sarkar, Phys. Rev. B **100**, 165413 (2019).
[17] A. M. Jones, H. Yu, J. S. Ross, P. Klement, N. J. Ghimire, J. Yan, D. G. Mandrus, W. Yao, and X. Xu, Nat. Phys. **10**, 130 (2014).
[18] H. Su, C. Wei, A. Deng, D. Deng, C. Yang, and J.-F. Dai, Nanoscale **9**, 5148 (2017).
[19] R. Suzuki, M. Sakano, Y. J. Zhang, R. Akashi, D. Morikawa, A. Harasawa, K. Yaji, K. Kuroda, K. Miyamoto, T. Okuda, K. Ishizaka, R. Arita, and Y. Iwasa, Nat. Nanotechnol. **9**, 611 (2014).
[20] R. Akashi, M. Ochi, S. Bordács, R. Suzuki, Y. Tokura, Y. Iwasa, and R. Arita, Phys. Rev. Appl. **4**, 014002 (2015).
[21] L. Du, J. Tang, J. Liang, M. Liao, Z. Jia, Q. Zhang, Y. Zhao, R. Yang, D. Shi, L. Gu, J. Xiang, K. Liu, Z. Sun, and G. Zhang, Research **2019**, 6494565 (2019).
[22] H. Yuan, M. S. Bahramy, K. Morimoto, S. Wu, K. Nomura, B.-J. Yang, H. Shimotani, R. Suzuki, M. Toh, C. Kloc, X. Xu, R. Arita, N. Nagaosa, and Y. Iwasa, Nat. Phys. **9**, 563 (2013).
[23] D. Xiao, G.-B. Liu, W. Feng, X. Xu, and W. Yao, Phys. Rev. Lett. **108**, 196802 (2012).
[24] J. R. Schaibley, H. Yu, G. Clark, P. Rivera, J. S. Ross, K. L. Seyler, W. Yao, and X. Xu, Nat. Rev. Mater. **1**, 16055 (2016).
[25] X. Jun, Z. Mervin, W. Yuan, and Z. Xiang, Nanophoton. **6**, 1309 (2017).
[26] T. Cao, G. Wang, W. Han, H. Ye, C. Zhu, J. Shi, Q. Niu, P. Tan, E. Wang, B. Liu, and J. Feng, Nat. Commun. **3**, 887 (2012).
[27] Y. J. Wu, C. Shen, Q. H. Tan, J. Shi, X. F. Liu, Z. H. Wu, J. Zhang, P. H. Tan, and H. Z. Zheng, Appl. Phys. Lett. **112**, 153105 (2018).
[28] A. Srivastava, M. Sidler, A. V. Allain, D. S. Lembke, A. Kis, and A. Imamoğlu, Nat. Phys. **11**, 141 (2015).
[29] D. MacNeill, C. Heikes, K. F. Mak, Z. Anderson, A. Kormányos, V. Zólyomi, J. Park, and D. C. Ralph, Phys. Rev. Lett. **114**, 037401 (2015).
[30] Y. Li, J. Ludwig, T. Low, A. Chernikov, X. Cui, G. Arefe, Y. D. Kim, A. M. van der Zande, A. Rigosi, H. M. Hill, S. H. Kim, J. Hone, Z. Li, D. Smirnov, and T. F. Heinz, Phys. Rev. Lett. **113**, 266804 (2014).
[31] J. M. Lu, O. Zheliuk, I. Leermakers, N. F. Q. Yuan, U. Zeitler, K. T. Law, and J. T. Ye, Science **350**, 1353 (2015).
[32] N. Li, J. Zhang, Y. Xue, T. Zhou, and Z. Yang, Phys. Chem. Chem. Phys. **20**, 3805 (2018).
[33] Y. Song, Q. Zhang, W. Mi, and X. Wang, Phys. Chem. Chem. Phys. **18**, 15039 (2016).
[34] X. Wu, J. Zhou, P. Li, Y. Wu, Z. Wu, X. Li, and J. Kang, J. Phys. D **53**, 125104 (2020).
[35] Q. Zhang, S. A. Yang, W. Mi, Y. Cheng, and U. Schwingenschlögl, Adv. Mater. **28**, 959 (2016).
[36] Y. Ma, L. Kou, A. Du, B. Huang, Y. Dai, and T. Heine, Phys. Rev. B **97**, 035444 (2018).
[37] F. A. Rasmussen and K. S. Thygesen, J. Phys. Chem. C **119**, 13169 (2015).
[38] G. Kresse and J. Furthmüller, Comput. Mater. Sci. **6**, 15 (1996).
[39] G. Kresse and J. Furthmüller, Phys. Rev. B **54**, 11169 (1996).
[40] P. E. Blöchl, Phys. Rev. B **50**, 17953 (1994).
[41] J. P. Perdew, K. Burke, and M. Ernzerhof, Phys. Rev. Lett. **77**, 3865 (1996).

[42] Y. Sun, B. Xu, and L. Yi, Chin. Phys. B **29**, 023102 (2020).

[43] H. U. Din, M. Idrees, A. Albar, M. Shafiq, I. Ahmad, C. V. Nguyen, and B. Amin, Phys. Rev. B **100**, 165425 (2019).

[44] Q. Yang, S. Zhang, C. Tan, H. Ye, X. Ming, S. Ingebrandt, and X. Chen, J. Mater. Chem. C **5**, 9412 (2017).

[45] U. Herath, P. Tavadze, X. He, E. Bousquet, S. Singh, F. Muñoz, and A. H. Romero, Comput. Phys. Commun. **251**, 107080 (2020).

[46] See Supplemental Material at http://link.aps.org/supplemental/10.1103/PhysRevB.102.125414 for interlayer binding energy formulation, atomic orbital projected band structure, band structure of WSe_2 with and without SOC, variation in interlayer binding energy with interlayer in HfN_2/WSe_2 van der Waals heterostructure (vdWH), band structure in different stacking order in the vdWH, deformation potential plots, elastic constants and carrier mobility in HfN_2/WTe_2 vdWH.

[47] Y. Liu, Y. Gao, S. Zhang, J. He, J. Yu, and Z. Liu, Nano Res. **12**, 2695 (2019).

[48] D. Xiao, M.-C. Chang, and Q. Niu, Rev. Mod. Phys. **82**, 1959 (2010).

[49] D. J. Thouless, M. Kohmoto, M. P. Nightingale, and M. den Nijs, Phys. Rev. Lett. **49**, 405 (1982).

[50] M. Gradhand, D. V. Fedorov, F. Pientka, P. Zahn, I. Mertig, and B. L. Györffy, J. Phys. Condens. Matter **24**, 213202 (2012).

[51] H.-J. Kim, C. Li, J. Feng, J.-H. Cho, and Z. Zhang, Phys. Rev. B **93**, 041404(R) (2016).

[52] L. Xie and X. Cui, Proc. Natl. Acad. Sci. **113**, 3746 (2016).

[53] K. F. Mak, D. Xiao, and J. Shan, Nat. Photonics **12**, 451 (2018).

[54] T. Cao, M. Wu, and S. G. Louie, Phys. Rev. Lett. **120**, 087402 (2018).

[55] X. Zhang, W.-Y. Shan, and D. Xiao, Phys. Rev. Lett. **120**, 077401 (2018).

[56] N. Jena, Dimple, S. D. Behere, and A. De Sarkar, J. Phys. Chem. C **121**, 9181 (2017).

[57] M. Z. Hasan and C. L. Kane, Rev. Mod. Phys. **82**, 3045 (2010).

[58] Y. Wan, J. Xiao, J. Li, X. Fang, K. Zhang, L. Fu, P. Li, Z. Song, H. Zhang, Y. Wang, M. Zhao, J. Lu, N. Tang, G. Ran, X. Zhang, Y. Ye, and L. Dai, Adv. Mater. **30**, 1703888 (2018).

[59] C. Jiang, W. Xu, A. Rasmita, Z. Huang, K. Li, Q. Xiong, and W. Gao, Nat. Commun. **9**, 753 (2018).

[60] M. Z. Maialle, E. A. de Andrada e Silva, and L. J. Sham, Phys. Rev. B **47**, 15776 (1993).

[61] K. Hao, G. Moody, F. Wu, C. K. Dass, L. Xu, C.-H. Chen, L. Sun, M.-Y. Li, L.-J. Li, A. H. MacDonald, and X. Li, Nat. Phys. **12**, 677 (2016).

[62] C. R. Zhu, K. Zhang, M. Glazov, B. Urbaszek, T. Amand, Z. W. Ji, B. L. Liu, and X. Marie, Phys. Rev. B **90**, 161302(R) (2014).

[63] P. Rivera, K. L. Seyler, H. Yu, J. R. Schaibley, J. Yan, D. G. Mandrus, W. Yao, and X. Xu, Science **351**, 688 (2016).

[64] P. Rivera, J. R. Schaibley, A. M. Jones, J. S. Ross, S. Wu, G. Aivazian, P. Klement, K. Seyler, G. Clark, N. J. Ghimire, J. Yan, D. G. Mandrus, W. Yao, and X. Xu, Nat. Commun. **6**, 6242 (2015).

[65] M. K. Mohanta and A. De Sarkar, Appl. Surf. Sci. **526**, 146749 (2020).

[66] A. V. Krukau, O. A. Vydrov, A. F. Izmaylov, and G. E. Scuseria, J. Chem. Phys. **125**, 224106 (2006).

[67] F. Li, W. Wei, H. Wang, B. Huang, Y. Dai, and T. Jacob, J. Phys. Chem. Lett. **10**, 559 (2019).

[68] W. Feng, Y. Yao, W. Zhu, J. Zhou, W. Yao, and D. Xiao, Phys. Rev. B **86**, 165108 (2012).

[69] X. Hong, J. Kim, S.-F. Shi, Y. Zhang, C. Jin, Y. Sun, S. Tongay, J. Wu, Y. Zhang, and F. Wang, Nat. Nanotechnol. **9**, 682 (2014).

[70] J. Kim, C. Jin, B. Chen, H. Cai, T. Zhao, P. Lee, S. Kahn, K. Watanabe, T. Taniguchi, S. Tongay, M. F. Crommie, and F. Wang, Sci. Adv. **3**, e1700518 (2017).

[71] Moh. A. U. Absor, H. Kotaka, F. Ishii, and M. Saito, Phys. Rev. B **94**, 115131 (2016).

[72] M. K. Mohanta, A. Rawat, N. Jena, R. Ahammed, and A. D. Sarkar, J. Phys. Condens. Matter **32**, 355301 (2020).

[73] M. K. Mohanta, Dimple, A. Rawat, N. Jena, R. Ahammed, and A. D. Sarkar, Physica E **124**, 114222 (2020).

[74] V. Wang, N. Xu, J.-C. Liu, G. Tang, and W. T. Geng, arXiv:1908.08269.

[75] R. C. Andrew, R. E. Mapasha, A. M. Ukpong, and N. Chetty, Phys. Rev. B **85**, 125428 (2012).

[76] S. Singh, C. Espejo, and A. H. Romero, Phys. Rev. B **98**, 155309 (2018).

[77] H. Lang, S. Zhang, and Z. Liu, Phys. Rev. B **94**, 235306 (2016).

[78] Y. Wang and Y. Ding, J. Phys. Chem. C **122**, 26748 (2018).

[79] J. Dai and X. C. Zeng, Angew. Chem. **127**, 7682 (2015).

[80] J. Bardeen and W. Shockley, Phys. Rev. **80**, 72 (1950).

[81] M. K. Mohanta, A. Rawat, N. Jena, Dimple, R. Ahammed, and A. De Sarkar, ACS Appl. Mater. Interfaces **12**, 3114 (2020).

[82] M. K. Mohanta, A. Rawat, Dimple, N. Jena, R. Ahammed, and A. De Sarkar, Nanoscale **11**, 21880 (2019).

[83] M. K. Mohanta and A. D. Sarkar, ACS Appl. Mater. Interfaces **12**, 18123 (2020).